Frequency-dependent effects on travel times and waveforms of long-period S and SS waves: implications for the scale of mantle heterogeneity from finite-difference simulations

Heiner Igel, Institute of Theoretical Geophysics, Cambridge, UK
Oli Gudmundsson, Research School of Earth Sciences, Canberra, Australia

Abstract

The spectral properties of upper-mantle velocity perturbations are controversial. While global Earth models obtained by tomographic inversion are characterized by the dominance of long-wavelength features, results from regional tomography, and stochastic analysis of travel times suggest the presence of more power at intermediate scales than predicted by global models. We study frequency-dependent effects of long-period S and SS waves of SH-type through random upper-mantle models with specified spectral properties. Wave propagation is simulated by a finite-difference approximation to the axisymmetric wave equation in spherical coordinates. For global models with cylindrical symmetry and constant angular increment $\Delta\theta$ the use of spherical coordinates leads to an effective lateral grid spacing (arc length) decreasing with depth. This is contrary to the requirements of global models with low velocities at the top of the mantle, which necessitate a dense grid spacing at small depths and a wider grid spacing at the base of the mantle. We introduce a grid with depth-dependent lateral grid spacing to overcome this inconsistency. Our simulations suggest that (1) the properties of spatial power spectra of travel-time fluctuations are frequency dependent; (2) power spectra of models obtained from long-period tomography may underestimate the power at intermediate scales; (3) frequency-dependent effects on the waveform are sensitive to the scales and amplitudes of perturbations present in the upper mantle.

Keywords: mantle structure, finite differences, S and SS waves

1 Introduction

Determining the spectrum of heterogeneities in the Earth's mantle is important to constrain the types of convection present in the mantle and to understand the origin of modeled seismic-velocity anomalies. Spectral properties of mantle structure can be estimated from three-dimensional (3D) models obtained by global tomography or they can be estimated directly from observed travel-time fluctuations. A detailed comparison of power spectra for different global and regional models can be found in Passier and Snieder (1995). A discussion of global mantle models is given in Ritzwoller and Lavely (1995).

The spectral properties of mantle-velocity perturbations determined by various methods often differ substantially (Passier and Snieder, 1995). While tomographic images obtained from global-data inversion suggest a sharp onset of spectral decay at harmonic degree $l \approx 8$ (e.g. Su and Dziewonski, 1992; Zhang and Tanimoto, 1991, 1993; Pollitz, 1994) results from regional tomography (e.g. Snieder, 1988; Zielhuis and Nolet, 1994; Spakman et al., 1993) and stochastic analysis of travel times (Gudmundsson et al., 1990; Davies et al., 1992) indicate that there is more power in intermediate-scale heterogeneity than predicted by global inversions. These differences are attributed to (1) varied effects of the inversion schemes (e.g. Laske, Masters and Zürn, 1994); (2) complexity of the regions where regional tomography is carried out (Passier and Snieder, 1995); (3) filtering effects of finite-frequency propagation on travel times (Gudmundsson and Cummins, 1994).

To understand frequency-dependent effects on the determination of spectral properties we perform full-wavefield calculations for mantle models with known spectral properties. The numerical method we use is an extension of the finite-difference (FD) approach by Igel and Weber (1995, 1996) to grids with depth-dependent, lateral grid spacing. Grid refinement near the Earth's surface considerably improves the performance of the FD algorithm because (1) low velocities (small wavelengths) at the top of the mantle can be sampled more efficiently, and (2) higher velocities in the lower mantle are sampled less densely, improving stability.

The purpose of this paper is to present an FD algorithm with depth-dependent, lateral grid spacing for global, toroidal wave propagation, to discuss its accuracy, and to simulate frequency-dependent waveform effects for upper-mantle models with specified spectral properties.

2 Numerical algorithm

The algorithm presented in this paper is an extension of the high-order FD scheme of Igel and Weber (1995) to grids with radially varying grid spacing. The equations of motion in spherical coordinates r, θ, φ are solved for wavefields and media invariant in φ, thus rotationally symmetric with respect to the axis $\theta = 0$. For spherical or polar grids with equal spacing in the angular domain, the grid is coarse for large radii and dense near the centre. This is contrary to what is required for global Earth models. The velocities near the Earth's surface are considerably lower than deeper within the Earth and therefore require dense rather than coarse sampling. In addition, heterogeneities are clearly strongest in the lithosphere and uppermost mantle (possibly with the exception of the lowermost mantle, D") which consequently should be sampled with a dense grid.

2.1 Theory

Assuming invariance in φ the equations for toroidal motion u_φ are (e.g. Lapwood and Usami, 1981, sections 2.3 and 5.1)

$$\rho \frac{\partial^2 u_\varphi}{\partial t^2} = f_\varphi + \frac{\partial \sigma_{r\varphi}}{\partial r} + \frac{1}{r}\frac{\partial \sigma_{\theta\varphi}}{\partial \theta} + \frac{3}{r}\sigma_{r\varphi} + \frac{2}{r}\sigma_{\theta\varphi}\cot\theta \quad , \tag{1}$$

where ρ is the mass density, f_φ is a volumetric force, σ_{ij} are the components of the symmetric stress tensor,

$$\sigma_{r\varphi} = \mu\ (\frac{\partial u_\varphi}{\partial r} - \frac{1}{r}u_\varphi) \quad , \qquad \sigma_{\theta\varphi} = \frac{\mu}{r}(\frac{\partial u_\varphi}{\partial \theta} - \cot\theta\ u_\varphi) \quad , \tag{2}$$

μ being the shear modulus.

2.2 Discretization

All space dependent fields – stress, sources, and displacement – are defined on a spherical, staggered grid. Staggered grids have been used widely in isotropic (e.g. Virieux, 1984; 1986) and anisotropic (Igel et al., 1995) FD wavefield calculations. In staggered grids, the elements of displacement, stress, and strain are not defined at the same locations, allowing the first derivatives of those fields to be centered in between grid points. Due to the antisymmetry

of the difference operator, this improves the accuracy of the finite-difference calculation for a given space increment.

The spherical grid is shown schematically in Figure 1. The grid is defined between the Earth's surface and the core-mantle boundary (CMB). These two boundaries are modeled as free surfaces. To implement this boundary condition, the grid is extended $L/2 + 1$ levels above and below the physical boundary, L being the length of the FD differential (and interpolation) operator.

In the toroidal case with constant grid spacing in both the angular and the radial direction this leads to a consistent scheme without requiring additional interpolations. However, to link the two domains with different lateral grid spacing, interpolations are required at or around the depth of the grid change.

The free-surface boundary condition

$$\sigma_{r\varphi} = 0 \text{ at r } = 6371\text{km, and r } = 3480\text{km,} \tag{3}$$

is implemented by imposing symmetry of u_φ and antisymmetry of the $\sigma_{r\varphi}$ component with respect to the free surface(s).

As shown in Figure 1, the elements defined at $\theta = 0$ are the displacement u_φ and the stress element $\sigma_{r\varphi}$. At $\theta = 0$ the equation of motion are singular and the displacement field can not be evaluated. However, by symmetry we impose $u_\varphi = \sigma_{r\theta} = 0$. Analogous to the situation at the free surface the grid is extended $L/2 + 1$ points across the boundary $\theta = 0$ and the boundary condition is imposed by anti-symmetry of both stress and displacement field. The equivalent condition is imposed at the boundary $\theta = \pi$.

The source region near $\theta = 0$ is schematically shown in Figure 2. Our goal is to model point-source-like behavior. To achieve this, sources are input at a grid point close to the axis of symmetry. A directional force would thus result in a ring source (pure toroidal motion) with radiation pattern similar to a strike slip source but with an amplitude behavior $\propto \cos^2\theta$ rather than $\cos\theta$. The radiation pattern of such a source is unrealistic. Nevertheless, it allows us to study model-dependent wave phenomena where the source radiation pattern is irrelevant.

The motivation for changing the angular grid spacing was given above. Jastram and Tessmer (1994) and Rodrigues (1993) both introduced FD grids with vertically varying grid spacing, condensing the (cartesian) grid near the surface by a factor of 3. The stability of explicit FD algorithms is generally

of the form $c_{max}\frac{dt}{dx} \leq const.$, where c_{max} is the maximum velocity, and dt and dx are time increment and grid spacing, respectively. Depending on the actual velocity model, the time step has to be decreased in accordance with the change in grid spacing to keep the same level of stability. We find a change of lateral grid spacing by a factor of 2 optimal for global models taking account of computation time.

The partial differentials and the interpolations are calculated by high-order operators of length L. The weights of the operators were obtained following the approach of Holberg (1987). The time evolution is carried out by a Taylor expansion. Details of this type of FD algorithm applied to wave propagation on a 3D cartesian grid can be found in Igel et al. (1995). In all simulations carried out in this paper we use 8-point space operators ($L = 8$) for both derivative and interpolation. The time extrapolation is accurate to fourth order.

3 Comparison with other methods

3.1 Spherically symmetric media

Before applying our algorithm to arbitrarily heterogeneous models we compare FD synthetic seismograms with those obtained by an *exact* method (Direct Solution Method (DSM), Geller et al., 1994; Cummins et al., 1994) for spherically symmetric media. The FD grid is divided into two domains with depth ranges 0-320 km and 320-2891 km, with grid sizes 2048×64 and 1028×512, respectively. The angular domain is 0-π and the time increment is 0.3 seconds. The model is the isotropic part of PREM (Dziewonski and Anderson, 1981).

In Figure 3 seismograms are compared for two epicentral distances at a period of 20 seconds. The source (toroidal ring source) is at 200 km depth. The overall agreement between the entirely different numerical techniques is excellent. Small phase differences are attributed to the discreteness of the FD grid, which can be suppressed by further grid refinements. The relative amplitude of the phases as well as the waveforms are well modeled by the FD approximation.

How does the grid refinement near the surface improve the performance of the FD scheme? To demonstrate the performance of the suggested algorithm

we undertake a convergence test. We compare seismograms from three different simulations: I. Reference seismogram obtained with a very dense grid (5120×1024); II: Seismogram for a 1024×256 grid; III: same as II, but with a 2048×32 refined grid at the top 360 km of the model.

The algorithm allows us to calculate the response of the model to a source time function of the form

$$f_\varphi(r,\theta,t) \;=\; \delta(\theta-\theta_s)\;\delta(r-r_s)\;\delta(t-t_s) \quad , \tag{4}$$

where we define the discrete delta functions as

$$\begin{aligned}
\delta(\theta) &= \begin{cases} 1/(\mathrm{r_s d}\theta) & \text{at } \theta=\theta_s \\ 0 & \text{otherwise} \end{cases} \\
\delta(r) &= \begin{cases} 1/\mathrm{dr} & \text{at r=r}_s \\ 0 & \text{otherwise} \end{cases} \\
\delta(t) &= \begin{cases} 1/\mathrm{dt} & \text{at t=t}_s \\ 0 & \text{otherwise} \end{cases} \quad ,
\end{aligned} \tag{5}$$

where dr and dθ are the space and dt the time increments, and θ_s, r_s, and t_s are the source coordinates.

The resulting seismograms are later convolved with a source wavelet of the desired frequency band. The wavelet is given by

$$S(t) \;=\; \sin[n\pi\frac{t}{T}] \;-\; \frac{n}{n+2}\sin[(n+2)\pi\frac{t}{T}] \quad , \qquad 0\le t\le T \quad , \tag{6}$$

where n is the number of sides and T is the dominant period. In all our simulations $n=2$. This allows us to study the convergence of the FD solution to the *correct* solution as a function of grid size (e.g. with or without refinement near the surface). In Figure 4 seismograms are shown for three different dominant periods at a distance of 80° . At the considered frequencies the seismograms obtained for the coarse grid are accurate for periods $\geq$60 seconds while the grid refinement enables the calculation of accurate seismograms down to a period of $\approx$25 seconds. The increase of CPU time for the simulation of type III with respect to type II was 30%. However, as Figure 4 indicates, a substantial improvement in accuracy results.

3.2 Travel-time accuracy for 2-D model

A further demonstration of the accuracy is given by a comparison of travel times derived from the FD seismograms with those obtained by the Huygens method (Witte et al., 1996). The 2-D model is generated by adding lateral perturbations to the isotropic part of PREM. The lateral S-velocity perturbations are shown in Figure 5a. The perturbations are coherent down to a depth of 250km where they are tapered to zero. The perturbations are also zero in the vicinity of the axis $\theta = 0$ to avoid interference due to the axi-symmetry of the model.

Travel times for the S ($S_{\rm diff}$) phase from the FD seismograms were obtained by maximizing cross-correlation between perturbed and unperturbed seismograms for a period of 30 seconds. Comparison of the travel-time perturbations obtained by these different approaches are shown in Figure 5b. The sampling rate of the FD seismograms is 2/3 seconds and the receiver spacing is 1/3 degrees. The maximum difference between the ray-theoretical and FD travel time is $\approx$1 second.

Since the direct S ($S_{\rm diff}$) phase is arriving at a very steep angle, we expect anti-correlation between velocity and travel-time perturbation, which can be appreciated by comparing Figures 5a and 5b.

The accuracy of our algorithm as far as waveforms and travel times are concerned gives us confidence that we can apply our FD method to study finite-frequency amplitude and waveform effects.

4 Spectra of mantle models

The aim of this study is to investigate the frequency dependence of travel times and waveforms of S and SS waves for upper-mantle models with varied power spectra and the implications for the scale of mantle heterogeneity. A schematic representation of the power spectrum of mantle-velocity perturbations is shown in Figure 6. The two types of spectra shown in this Figure (type I and type II) represent extreme cases of Passier and Snieder (1995). They showed that at intermediate scales (l=30) the spectra obtained by global and regional inversions differ by as much as a factor of 10-30. One of their arguments for the presence of significant intermediate-scale heterogeneity is the complexity of long-period surface-wave spectra due to multipathing

and the associated interference effects.

We generate models with type I and II statistics shown in Figure 6. Details of the model generation are given in the Appendix. Figure 7 shows 5 random model realizations of each spectral type. Clearly spectral type I contains mainly continent-scale features while type II contains a significant amount of energy at scales down two ≈ 100 km wavelength.

To test the spectral properties of the synthetic models we average the power spectra of several realizations for each type. Numerical tests show that at least 5 power spectra of different realizations have to be summed to achieve an accuracy of 5% for the decay rate. Results are shown in Figure 8. The power spectra display the characteristic corner frequency and the spectral decay which was imposed during the generation of the models.

2-D models of S-velocity perturbations are obtained by superimposing several lateral 1-D functions weighted by depth-dependent orthogonal functions. Details about the 2-D model generation are given in the Appendix. Sections of models thus obtained are shown in Figure 9. The S-velocity perturbations for all the simulations described below are tapered down to zero between 500km and 600km depth. There are no lateral velocity perturbations below 600km depth. It is important to note that the 2-D perturbations vanish near the axis of rotational symmetry $\theta = 0$ to avoid focusing effects. The perturbations are imposed for $\theta \geq 10^{\circ}$.

In the following we investigate synthetic seismograms obtained for the model types just described. All models have 2-D S-velocity perturbations according to spectral types I or II from Figure 6. The models considered below have maximum velocity perturbations of 12% corresponding to a root-mean-square perturbation of 3.2%.

4.1 Synthetic seismograms

We calculate synthetic seismograms for perturbations of types I and II added to the isotropic part of PREM with the following set-up. The mantle is sampled in depth by 578 grid points, leading to a depth spacing of 5.0km. The upper part of the mantle (0-320km depth) is defined on a grid of size 2560×64, while the bottom part (320-2891km depth) is defined on a 1280×512 grid. We focus on S and SS phases, which are frequently used in global tomographic studies. Seismograms of length 1 hour (12000 time steps with time increment $dt = 0.3s$) are calculated for epicentral distances 50-150° with a receiver

spacing of $1/3^o$. Windows containing S and SS arrivals are extracted using ray-theoretical travel times.

Seismograms for $S_{\rm diff}$ at a receiver sampling of 1 degree are shown in Figure 10 for a dominant period of 25 seconds for epicentral distances 100-150^o . The seismograms shown in Figure 10 were obtained for a 2-D realization of spectral types I (top) and II (bottom) for different maximum perturbation amplitudes. In the context of seismic-velocity anomalies and their relation to tectonic features the small and large perturbation amplitudes may represent regions of little (e.g. cratons) and high (e.g. island-arc regions) tectonic activity.

Concerning the $S_{\rm diff}$ phase we can make the following observations: (1) For model type I the S waveform is essentially undisturbed even for large perturbations; (2) for model type II the waveform begins to be affected by the scattering for perturbation amplitudes greater than 4%.

From the same set of seismograms we extract time windows containing the SS phase. These are shown in Figure 11. For model type I similar observations can be made as for the S ($S_{\rm diff}$) phase. The waveform – in the spherically symmetric case the Hilbert transform of the S phase (Choy and Richards, 1975) – is hardly affected by the velocity perturbations even at large perturbation amplitudes (12%). However, the SS-waveforms of model type II are severely distorted for perturbations larger than 4%. It is worth noting that most of the scattered energy in Figure 11 (bottom) is precursory to SS.

How does the waveform distortion depend on the dominant period of the wavelet used? For long-period wavelets (75 seconds) the situation is quite different (see Figure 12). Although there still is a considerable difference between the two model types, the waveforms for model type II are much less distorted than at a dominant period of 25 seconds. We try to quantify this frequency dependent $SS-$waveform distortion in the next section.

4.2 Frequency-dependent effects on the waveform

To describe the frequency-dependent scattering effect we process the SS-windows in the following way: (1) Find the time delay τ of the perturbed phase with respect to a reference (PREM) wavelet. (2) Correct the time delay and calculate a scattering index $s(T)$ (normalized root-mean-square dispacement misfit in a time window of length $2T$, T being the dominant

period) according to

$$s(T) = [\frac{1}{N} \sum_{receivers}^{N} \frac{1}{2T} \sum_{time}^{2T} \frac{(u_{pert}(T, t-\tau) - u_{ref}(T,t))^2}{u_{ref}^2(T,t)}]^{1/2} \ . \qquad (7)$$

This processing is carried out for the seismograms shown in Figures 11 and 12, for periods from 20-110 seconds and 50 receivers between 50° and 150° epicentral distance and for four other simulations with the corresponding spectral properties. For each model set-up the scattering index is thus averaged over 5 simulations. We suggest that the scattering index obtained for the different model types is representative for the particular spectral properties.

The results are shown in Figure 13. For spectral type I (Figure 13, left) even for large model perturbations (12%) the average waveform distortion does not exceed 7%. In the case of spectral type II (Figure 13, right) there is a rapid increase in waveform distortion for periods $\leq$30 seconds. In the long period limit the convergence of the perturbed and unperturbed waveforms is more rapid for models of type I.

4.3 Frequency-dependent effects on travel times

We now look at the frequency dependence of the spectrum of SS travel-time fluctuations measured at the surface. The model considered is of spectral type II (see Figure 6). The maximum perturbation amplitude is 6%, which is a likely underestimate of the strength of heterogeneity in the upper mantle judged by results of surface-wave tomography (e.g. Zielhuis and Nolet, 1994).

The dense and regular receiver sampling (1/3° between 50° and 150°) allows us to achieve high accuracy in the travel-time spectra at intermediate scales (l$\leq$ 300). The travel times are determined by maximizing the cross-correlation between perturbed and unperturbed SS waveforms. Travel times are picked from seismograms of three different dominant periods (25, 50, and 100 seconds). Examples are shown in Figure 14. While there is overall a good correlation between the travel-time fluctuations, they tend to be larger and show more details at shorter periods.

To obtain stable results for the travel-time spectra we sum power spectra from 5 different model realizations for each of the three frequency bands considered. The decay rate of the stacked power specta is determined by linear regression in the intervals indicated below.

At high frequencies (dominant period 25 seconds), the power spectrum of the travel-time fluctuations has the same decay rate as the underlying model perturbations. At 50 seconds dominant period the characteristics of the spectrum change. The onset of the decay is shifted towards lower harmonic degrees. In addition, the decay rate changes near harmonic degree l = 40. Up to harmonic degree 40 the decay is slightly faster than for the model perturbations, while for harmonic degrees above 40 the slope is greater by a factor of 2. These effects are even more pronounced at a dominant period of 100 seconds. The onset of the spectral decay seems to be shifted down to degree l=10. While the decay below l=35 reflects roughly the spectral properties of the velocity perturbations the decay beyond l=35 is much more pronounced.

It is instructive to consider the spectral ratio of the results shown in Figure 15. The spectra of the two longer-period travel-time fluctuations (50 and 100 seconds) are divided by the power spectrum obtained for a dominant period of 25 seconds. The results shown in Figure 16 further illustrate the dependence of the corner and decay of the spectra on the dominant period of the wave field propagating through the perturbed region.

5 Discussion and Conclusions

The goal of this study was to analyze full-wavefield, synthetic seismograms for random upper-mantle models with specified spectral properties and to investigate frequency-dependent effects on waveforms and travel times of S and SS waves.

The synthetic study we have undertaken is statistical in nature and requires a number of wave simulations to be carried out in order to achieve a stable estimate of spectra. Therefore, an efficient forward technique allowing us to model complete seismograms for arbitrary homogeneous structures was necessary. Accurate 3-D global simulations without assumptions on the amplitude of perturbations are still too expensive computationally. We compromise in using a FD approximation to the wave equation in spherical coordinates where all fields are invariant in φ. This leads to a 2-D problem which can be solved efficiently on present-day parallel computers.

We extended the FD algorithm suggested by Igel and Weber (1995) to grids with vertically-varying, lateral grid spacing. The grid refinement near

the Earth's surface is necessary from an algorithmic point of view (the arc length of the angular grid increment increases with distance from the center of the sphere) and from velocity model considerations (low velocities in the crust and lithosphere require smaller grid spacing). The change in grid spacing has been implemented using a high-order approximation. The relatively thin layer ($\leq$ 200km) with refined grid spacing leads to an additional 30% in computation time (as compared to a simulation without refinement). However, to achieve the same accuracy without grid refinement, simulations about four times longer would have been necessary. This is crucial for this study where the investigation of random structures and their spectral properties requires many simulations to be carried out.

The scale of seismic-velocity perturbations in the Earth's mantle is important in many aspects of geodynamics (e.g. mantle convection, subduction, hot spots, etc). In several studies, conclusions about mantle convection were drawn from power spectra of global tomographic models (e.g. Montagner and Tanimoto, 1991; Montagner 1994) or even directly from the power spectra of SS-traveltime fluctuations (e.g. Su and Dziewonski, 1991, 1992). In a recent study Passier and Snieder (1995) highlighted the discrepancy between the scales of velocity perturbations obtained from global and regional tomography.

In this study we attempted to use an accurate full wave field algorithm to examine the scattering effects of upper mantle models with known spectral properties. Our simulations can be classified according to the characteristics of the random velocity perturbations and the properties of the wavefield. As far as the scattering medium is concerned the relevant parameter is the correlation length. We define the correlation length a as double the half-width of the auto-correlation function of the lateral velocity perturbations. For our model types I and II this length was estimated as a_{I}=1600km and a_{II}=500km. The wave field is characterised by the dominant wavelength. We determine the dominant wavelength for an average mantle S-velocity of 5km/s. The thickness d of the scattering region is 550km.

In Figure 17 our SS-wave simulations are classified in terms of period and the length scales that control scattering phenomena: the scale length of heterogeneity and the widths of the relevant Fresnel zones. The Fresnel-zone width at the bounce point is calculated assuming an epicentral distance of 100 degrees and surface focus. The width of the Fresnel zone beneath the receiver is computed for the middle of the heterogeneous region, i.e. at a

depth of 275 km. We expect scattering effects or diffraction to be significant where the width of the first Fresnel zone exceeds the scale length of the inhomogeneity. Where the Fresnel zone is narrower than one correlation length we expect scattering effects to be insignificant, that ray theory apply, and that the spectral properties of the arrival-time fluctuations reflect the spectral properties of the velocity perturbations.

The classification of our simulations corresponds well with the results derived from the synthetic seismograms if we assume that the measured variations of time are dominated by contributions from the region immediately beneath the receiver. The widths of the Fresnel zones in the region beneath the receivers correspond to harmonic degrees l = 53, 39, and 29, respectively for dominant periods of 25, 50 and 100 seconds. For models of type I little power exists beyond harmonic degree 30 and as all the Fresnel-zone widths lie below the characteristic scale of the heterogeneity scattering effects are small. This interpretation agrees with the results of our simulations. For models of type II significant power exists up to degree 50. The width of the Fresnel zone for 25 second waves lies below the correlation length of the medium. We therefore expect the heterogeneity distribution to be mapped into the travel-time fluctuations unaffected. This is the result of our simulations (see Figure 15). At 50 seconds the Fresnel-zone width is comparable to one correlation length. We therefore expect a marginal effect as we do indeed observe in our simulations. At 100 seconds the Fresnel-zone width exceeds one correlation length and scattering effects are more significant.

It is interesting to compare the harmonic degree at which a bend appears in the spectra in Figure 15 to the harmonic degrees corresponding to the widths of the appropriate Fresnel zones. A bend occurs in the spectrum for 50 second waves at l=40-50. For 100 second waves a similar bend appears at l=30-40. This corresponds crudely with the calculated Fresnel-zone widths which translate into harmonic degrees l = 39 and 29 for 50 and 100 second waves respectively. This indicates that the apparent bends in the spectra in Figure 15 represent the onset of scattering/diffraction effects. No clear knee is evident in the spectrum for 25 second waves.

The above discussion ignores contributions to the travel-time fluctuations from the surface bounce point. The widths of the Fresnel zones at the bounce point correspond to harmonic degrees l = 3, 5, and 8 for 100, 50, and 25 second waves respectively. Thus we expect all travel-time signal carried by the SS waves from the bounce point to map into the lowest harmonics. That

signal therefore affects the spectrum marginally, although it may enhance the spectral plateau at low degrees somewhat in relative terms and thus artificially contribute to the spectral decay at around degree l=10.

We conclude that the travel-time fluctuations of long-period SS waves are dominated by structure beneath the recorder. Differential SS - S times effectively eliminate that contribution and carry the signature of structure beneath the bounce point of the SS wave. However, that signature is expected to be severely smoothed by scattering/diffraction effects.

Our synthetic modeling suggests that – as far as S, SS and $SS-S$ studies are concerned – the discrepancies reported by Passier and Snieder (1995) are at least in part due to finite-frequency effects of wave propagation. If the travel-time perturbations observed at the Earth's surface do not reflect the scale of the underlying mantle, it is impossible for delay-time tomography to model the power spectrum of mantle heterogeneity correctly. Similarly, if phase-velocities measured along the Earth's surface do not reflect the details of the structure of the mantle beneath, that detail cannot be recovered by inversion. Waveforms and amplitudes are necessary to model Earth structure in detail.

The results shown in Figure 13 suggest that the frequency-dependent effects on the waveform are sensitive to the scales and amplitudes of perturbations present in the upper mantle. This points to possible processing techniques which should be used in combination with travel-time processing when estimating the power spectrum of mantle velocity perturbations. Gudmundsson (1996) studied the effects of frequency on waveform distortion and travel-times. He concluded that – depending on the bandwidth – waveform distortion could be minor while diffraction effects on timing are significant. His results and our synthetic modeling suggest that even though waveform distortion may be significant, it may not be clear from a single seismogram (e.g. Figure 11).

The power spectra in Figure 15 demonstrate that the characteristics of the power spectra of SS travel-time fluctuations are frequency dependent. The slope of decay extracted from the power spectrum varies with the frequency band at which the power spectrum was determined. For example, at around $l = 100$ ($\approx$400km wavelength), the power spectrum determined at 25 seconds dominant period contains around 10 times more energy than the one determined at a dominant period of 50 seconds. This implies that conclusions on the scale of mantle heterogeneities from long-period seismograms

may be erroneous if these finite-frequency effects are not taken into account, e.g. by using more accurate complete wave field modeling.

It is important to note that – since our models are invariant in φ and thus two-dimensional – the effects we described in this paper are conservatively described. For 3-D models with the same spectral properties we expect the filtering effects to be even more pronounced.

Acknowledgements

We are grateful to the Centre National de Calcul Parallel en Science de la Terre (CNCPST) at the Institut de Physique du Globe de Paris for giving us access to the Connection Machine CM-5. One of the authors (HI) is funded by the NERC Grant GR3/10086. We are grateful to Phil Cummins for calculating the DSM seismograms and to Michael Roth for the Huygens arrival times. We thank Gerhard Müller, Fred Pollitz and Adam Schultz for helpful comments. We also thank M. Körnig and one anonymous reviewer for constructive reviews. Thanks to Brian Kennett for enabling HI to visit RSES; Contributions to this visit from Hughes Hall College, Cambridge are also acknowledged. Contribution No.XXXX of the Department of Earth Science and Institute of Theoretical Geophysics, University of Cambridge.

Appendix: Generation of velocity perturbations

We generate 1-D models with power spectral properties shown in Figure 6. Using the relation between wavenumber k and harmonic order l $kR = l+1/2$, R being the radius, we describe the amplitude spectrum as a function of harmonic order. Perturbations are then calculated according to the defined spectrum as follows

(1) generate a random (white) phase spectrum $[-\pi, \pi]$

(2) modulate complex phase spectrum with predefined amplitude spectrum to define the Fourier spectrum

(3) inverse FFT to obtain space domain representation

(4) scale to desired maximum perturbation.

(5) modulate perturbation with a prescribed function of depth.

Choises of amplitude (power) spectra and the depth modulation are described in the main body of the paper. Examples of perturbations calculated in this way are shown in Figure 7. (The analogy in 3D spherical coordinates would be to predefine the spherical-harmonic amplitude spectrum and distribute the power within each degree randomly among all its orders).

To make the models more realistic, incoherence in depth is introduced. Lateral perturbations are weighted with the set of depth-dependent functions

$$f_n(z) = 1, \quad n = 0.$$

$$f_n(z) = \sin(\frac{n\pi z}{h}), \quad n = 1, 3, ...$$

$$f_n(z) = \cos(\frac{n\pi z}{h}), \quad n = 2, 4, ... \tag{8}$$

and 2-D velocity perturbations $\Delta v_s(z, \theta)$ are obtained as

$$\Delta v_s(z, \theta) = \sum_{n=0}^{m} w_n g_n(\theta) f_n(z), \tag{9}$$

where $g_n(\theta)$ are the lateral perturbations, and w_n are weights. Examples of 2-D perturbations obtained for the spectra in Figure 6 are shown in Figure 9.

We use $m = 5$ for all 2-D models. For spectral type I the weights in equation (8) are $w_1 = w_2 = 1.0$, $w_3 = w_4 = 0.8$, $w_4 = w_5 = 0.4$, and for spectral type II all weights are unity.

References

Choy, G.L., and P.G. Richards, Pulse distortion and Hilbert transformation in multiply reflected and refracted body waves, *Bull. Seis. Soc. Am.*, 65, 55-70.

Cummins, P., R.J. Geller, T. Hatori, N. Takeuchi, DSM complete synthetic seismograms: SH, spherically symmetric case, *Geophys. Res. Let.*, 21, 1663-1666, 1994a.

Cummins, P., R.J. Geller, and N. Takeuchi, DSM complete synthetic seismograms: P-SV, spherically symmetric case, *Geophys. Res. Let.*, 21, 1663-1666, 1994b.

Davies, J.H., O. Gudmundsson, R.W. Clayton, Spectra of mantle shear velocity structure, *Geophys. J. Int.*, 108, 865-882, 1992.

Dziewonski, A., and D.L. Anderson, Preliminary reference Earth model, *Phys. Earth Planet. Int.*, *25*, 297-356, 1981.

Geller, R.J., and T. Ohminato, Computation of synthetic seismograms and their partial derivatives for heterogeneous media with arbitrary natural boundary conditions using the Direct Solution Method, *Geophys. J. Int*, 116, 421-446, 1994.

Gudmundsson, O., On the effect of diffraction on traveltime measurements, *Geophys. J. Int.*, 124, 304-314, 1996.

Gudmundsson, O., J.H. Davies, R.W. Clayton, Stochastic analysis of global traveltime data: mantle heterogeneity and random errors in the ISC data, *Geophys. J. Int.*, 102, 25-43, 1990.

Gudmundsson, O., P. Cummins, The importance of small-scale structure in the earth's upper mantle, AGU Fall Meeting 1994, Technical Programme, 1994.

Holberg, O., Computational aspects of the choice of operator and sampling interval for numerical differentiation in large scale simulation of wave phenomena, Geoph. Prosp., 35, 629-655, 1987.

Igel, H., and M. Weber, SH-wave propagation in the whole mantle using high-order finite differences, *Geophys. Res. Let.*, 22, 731-734, 1995.

Igel, H., M. Weber, P-SV wave propagation in the Earth's mantle using finite differences: Application to heterogeneous lowermost mantle structure, *Geophys. Res. Let.*, 23, 415-418, 1996.

Igel, H., P. Mora., and B. Riollet, Anisotropic wave propagation through FD grids, *Geophysics*, *60*, 1203-1216, 1995.

Jastram, C., E. Tessmer, Elastic modeling on a grid with vertically varying spacing, Geoph. Prosp., 42, 357-370, 1994.

Laske, G., G. Masters, W. Zürn, Frequency-dependent polarization anomalies of long-period surface waves and their implications for global phase-velocity maps, *Phys. Earth Planet. Inter.*, 84, 111-137, 1994.

Lapwood, E.R., T. Usami, Free oscillations of the Earth, Cambridge University Press, 1981.

Montagner, J.-P., Can seismology tell us anything about convection in the mantle?, Rev. Geoph., 32, 115-138, 1994.

Montagner, J.-P., T. Tanimoto, Global upper mantle tomography of seismic velocities and anisotropies, *J. Geophys. Res.*, 96, 20337-20351, 1991.

Passier M.L., R. Snieder, On the presence of intermediate-scale heterogeneity in the upper mantle, *Geophys. J. Int.*, 123, 817-837, 1995.

Pollitz, F.F. , Global tomography from Rayleigh and Love wave dispersion: effect of ray-path bending, *Geophys. J. Int.*, 118, 730-758, 1994.

Ritzwoller, M.H., E.M. Lavely, Three-dimensional seismic models of the Earth's mantle, Rev. Geophys., 33, 1-66, 1995.

Rodrigues, D., Simulation de la propagation d'ondes sismiques sur machine massivement parallèle, Thèse de l'Ecole Central de Paris, 1993.

Snieder, R., Large scale waveform inversions of surface waves for lateral heterogeneity: 2. Application to surface waves in Europe and the Mediterranean, *J. Geophys. Res.*, 93, 12067-12080, 1988.

Spakman, W., S. Van der Lee, R. Van der Hilst, Traveltime tomography of the European-Mediterranean mantle down to 1400km *Phys. Earth Planet. Inter.*, 79, 3-74, 1993.

Su, W.-J., A. Dziewonski, Predominance of long-wavelength heterogeneity in the mantle, Nature, 352, 121-126, 1991.

Su, W.-J., A. Dziewonski, On the scale of mantle heterogeneity, *Phys. Earth Planet. Inter.*, 74, 29-54, 1992.

Virieux, J., SH-wave propagation in heterogeneous media: velocity-stress finite-difference method, *Geophysics*, 49, 1933–1942, 1984.

Virieux, J., P-SV wave propagation in heterogeneous media: velocit-stress finite-difference method, *Geophysics*, 51, 889-901, 1986

Witte, O., M. Roth, G. Müller, Ray tracing in random media, *Geophys. J. Int.*, 124, 159-169. 1996.

Zielhuis, A., G. Nolet, Shear-velocity variations in the upper mantle beneath central Europe, 117, 695-715, 1994.

Zhang, Y.-S., T. Tanimoto, Global love wave phase velocity variation and its significance to plate tectonics, *Phys. Earth Planet. Inter.*, 66, 160-202 1991.

Zhang, Y.-S., T. Tanimoto, High resolution global upper mantle structure and plate tectonics, *Geophys. J. Int.*, 98, 9793-9823.

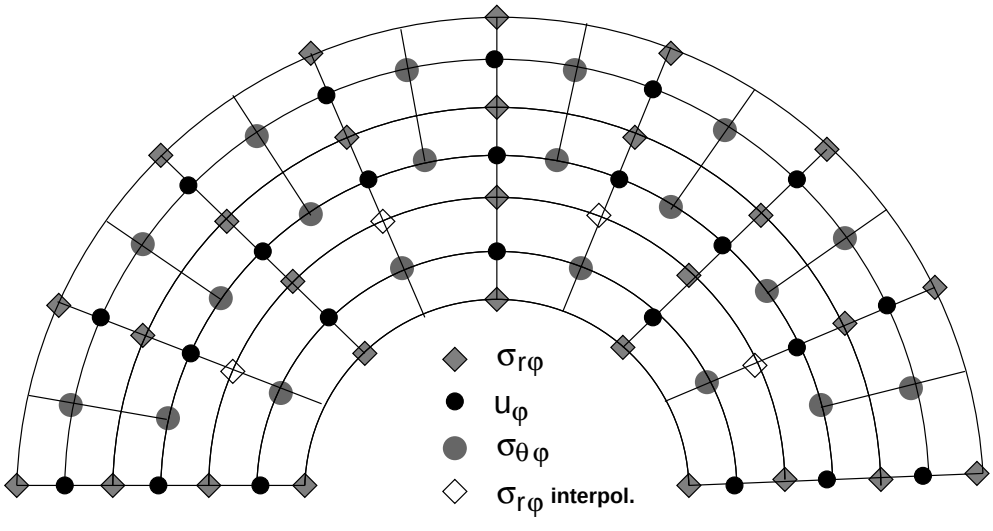

Figure 1: Staggered grid used in the FD scheme. At the top of the model the angular grid spacing $\Delta\theta$ is increased by a factor of 2. The radial grid spacing Δr is constant throughout the grid. The Earth's surface and the CMB are modeled with a free-surface boundary condition. At the level of changing angular grid spacing, $L/2$ levels of interpolated $\sigma_{r\theta}$ components have to be added to connect the two domains (L being the length of the space operator, for the purpose of this figure $L = 2$). The angular domain is 0-π.

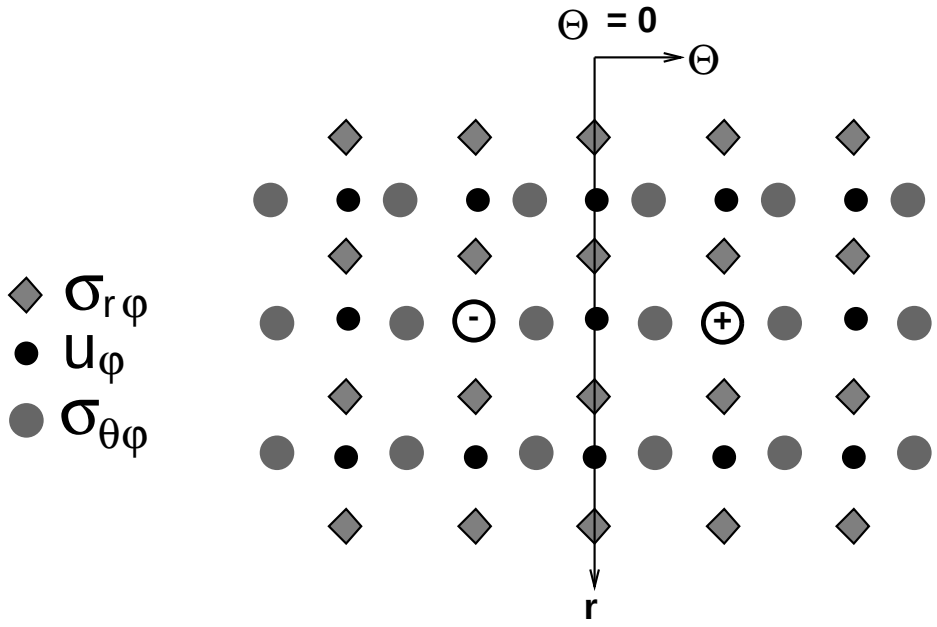

Figure 2: The staggered FD grid close to the axis $\theta = 0$. The equations of motion are singular at $\theta = 0$. At the axis of symmetry $u_\varphi = 0$ and $\sigma_{r\varphi} = 0$ are imposed by symmetry. Note that a directional force input at a grid point $(+)$ next to the axis of symmetry leads to a toroidal ring source. The grid is extended $L/2 + 1$ levels beyond $\theta = 0$, i.e. to the left, where L is the length of the space operator, to enforce the boundary condition. For the purpose of this graph $L = 4$.

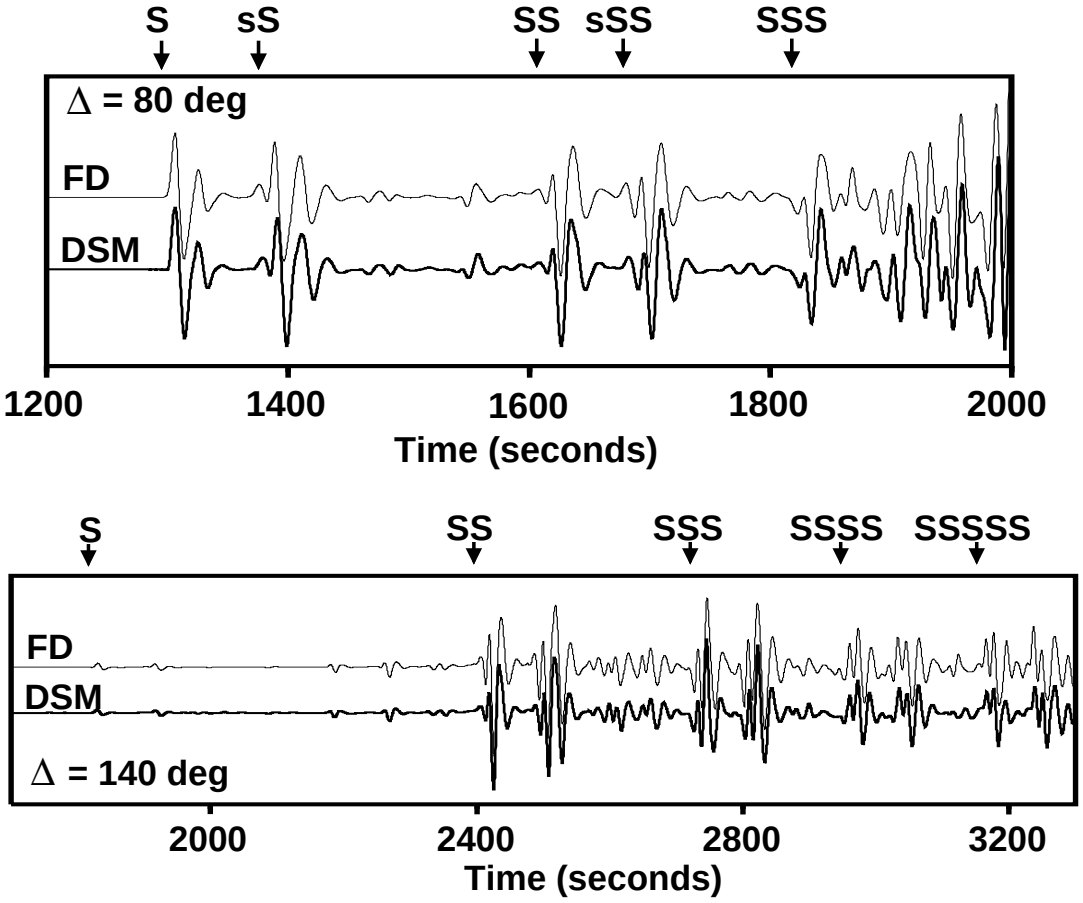

Figure 3: Comparison of DSM (bold) and FD seismograms for the isotropic part of PREM. The dominant period is 20 seconds. Some arrival times of S phases are marked by arrows. Top: Epicentral distance 80 degrees. (the direct arrival is a superposition of S and ScS). Bottom: 140 degrees.

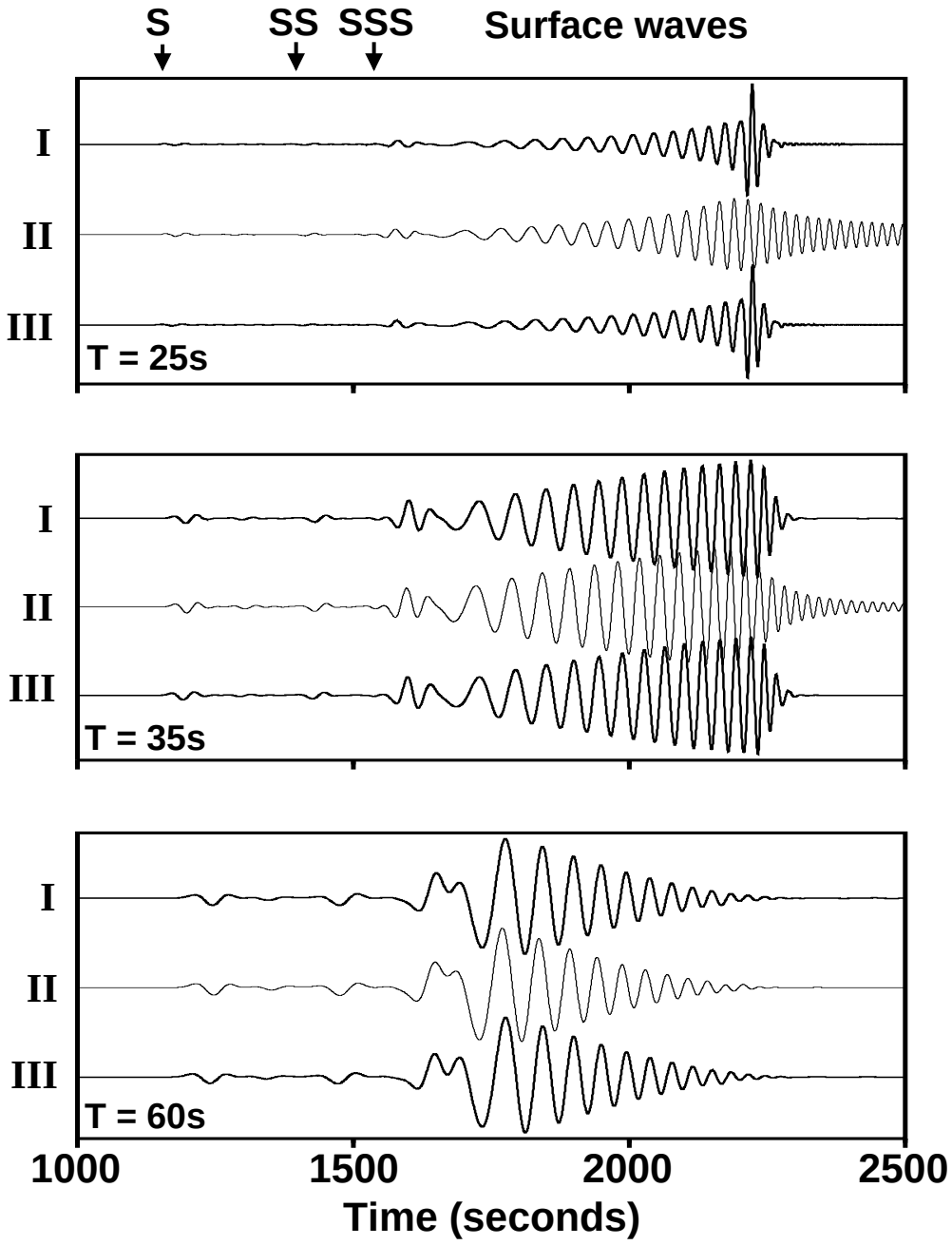

Figure 4: The effect of the change in grid spacing at the top of the model for different frequencies (25, 35, and 60 seconds dominant period). The source is at the surface. The model is the isotropic part of PREM. Arrival times of some phases are marked by arrows. For each frequency band three seismograms at an epicentral distance of 80° are shown: I. Reference seismogram obtained with a very dense grid (5120×1024); II: Seismogram for a 1024×256 grid; III: same as II, but with a 2048×32 refined grid at the top of the model. The accuracy of the surface waves is considerable improved by the grid refinement.

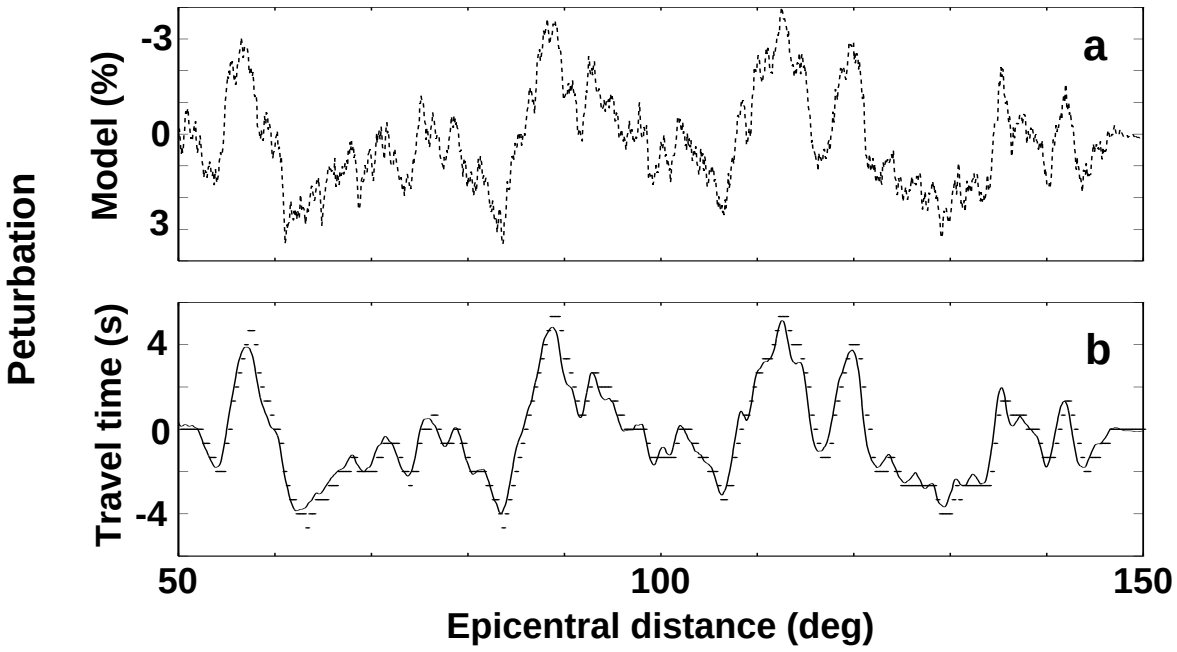

Figure 5: Top: Lateral velocity perturbations which were added to PREM at the top of the mantle. The perturbations are coherent down to a depth of 250 km. Bottom: Travel-time perturbations for S ($S_{\rm diff}$) obtained by the Huygens method (solid line, Witte et al., 1995), and those obtained with the FD method (dots). The sampling of the FD seismograms was 2/3 seconds.

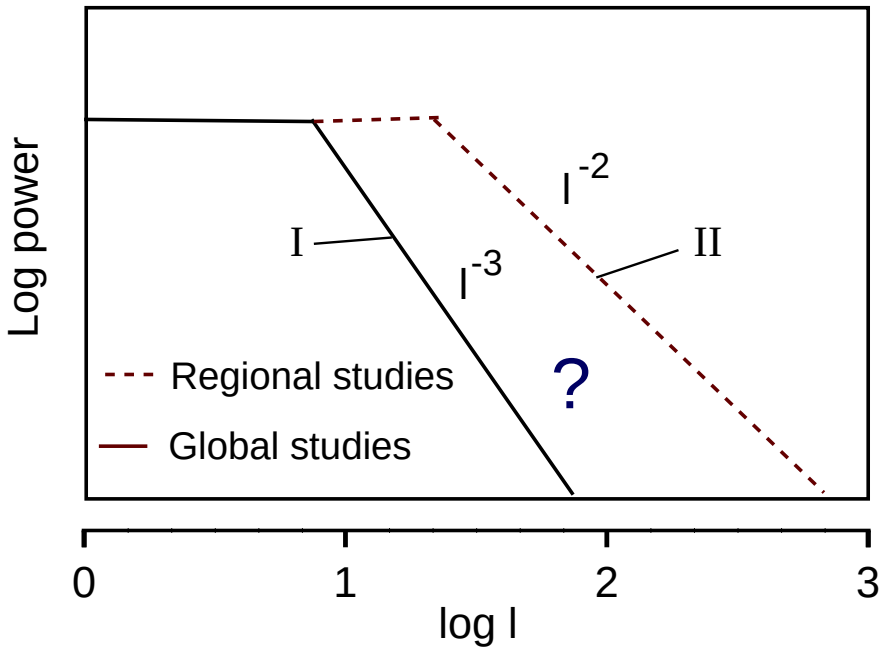

Figure 6: Power spectra of lateral velocity perturbations suggested by Passier and Snieder (1995) as representative of global tomographic models (type I, solid) and regional tomographic (and other) models (type II, dashed).

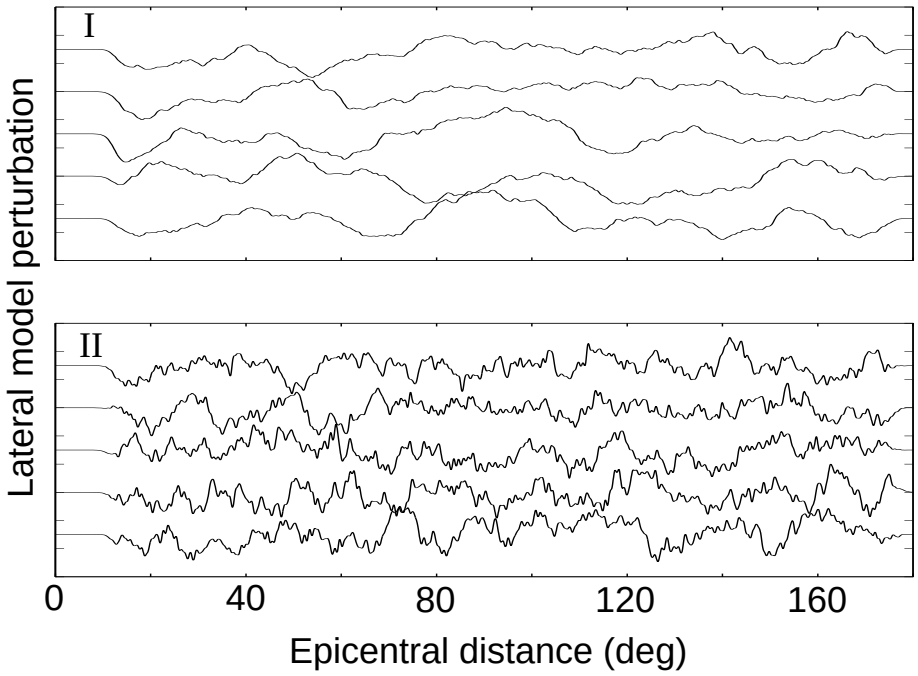

Figure 7: Realizations of models of lateral shear-velocity perturbations for the two types of spectra shown in the Figure 6.

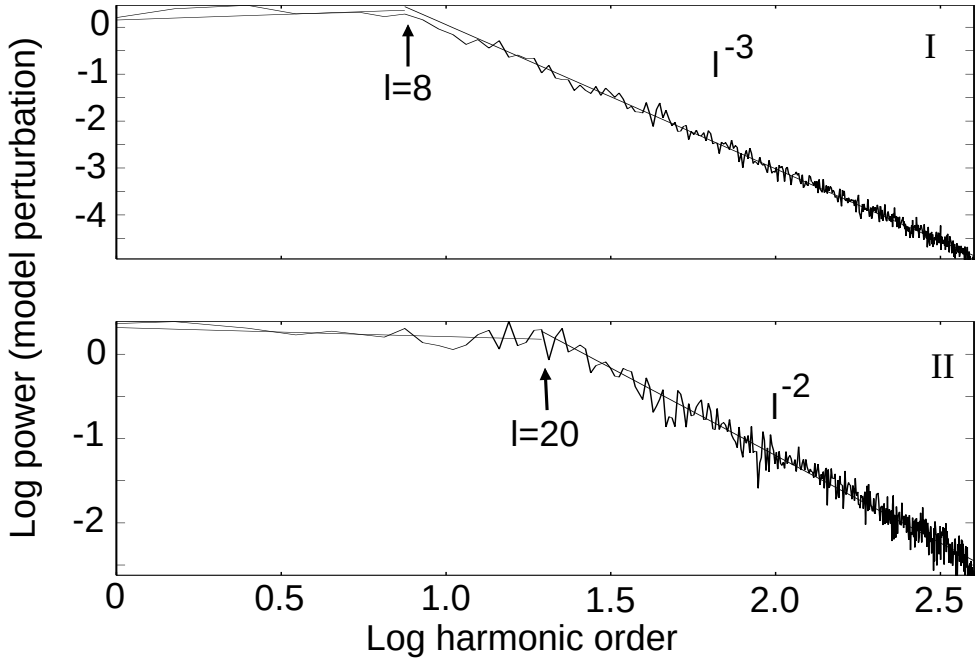

Figure 8: Power spectra obtained by stacking five spectra of the realizations shown in Figure 7. Straight lines correspond to linear regressions. The corner of spectral decay and the decay rate are well matched (the error of the slope is $\leq 5\%$).

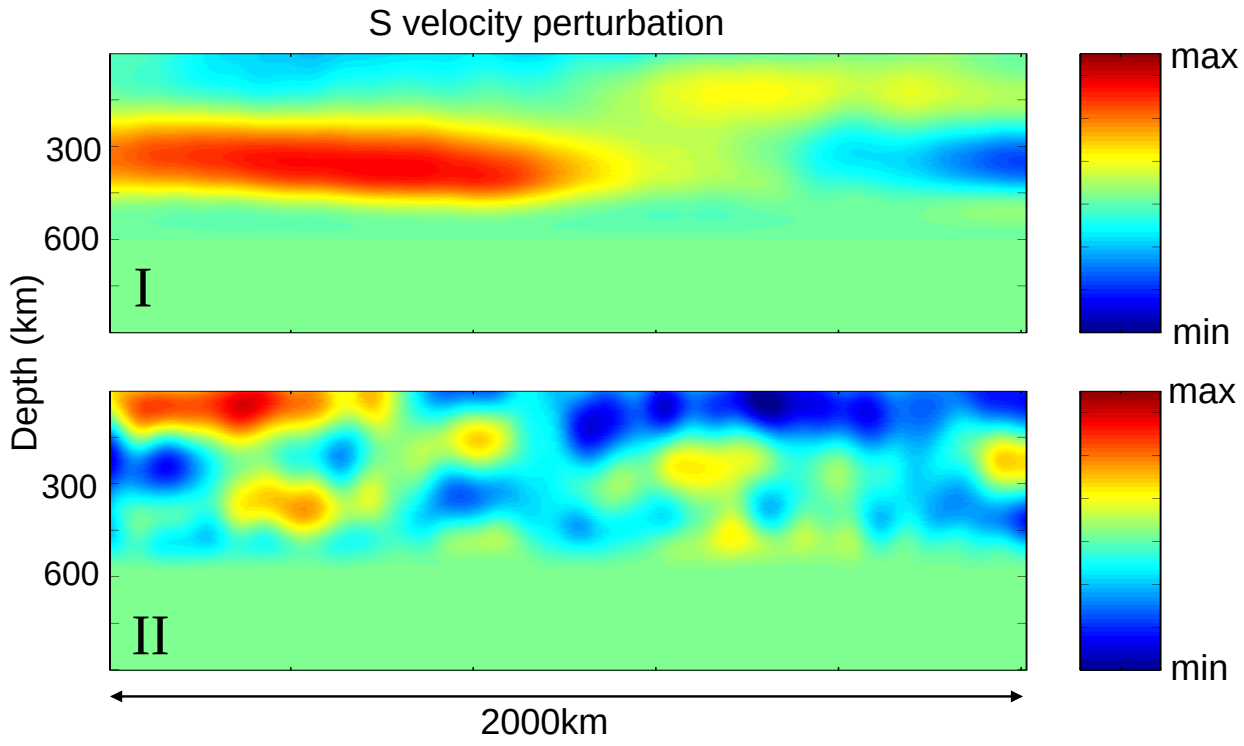

Figure 9: Two-dimensional models for the two types of power spectra. The perturbations are limited to the top 500 km. Top: type I; Bottom: type II. See text for details about the depth dependence.

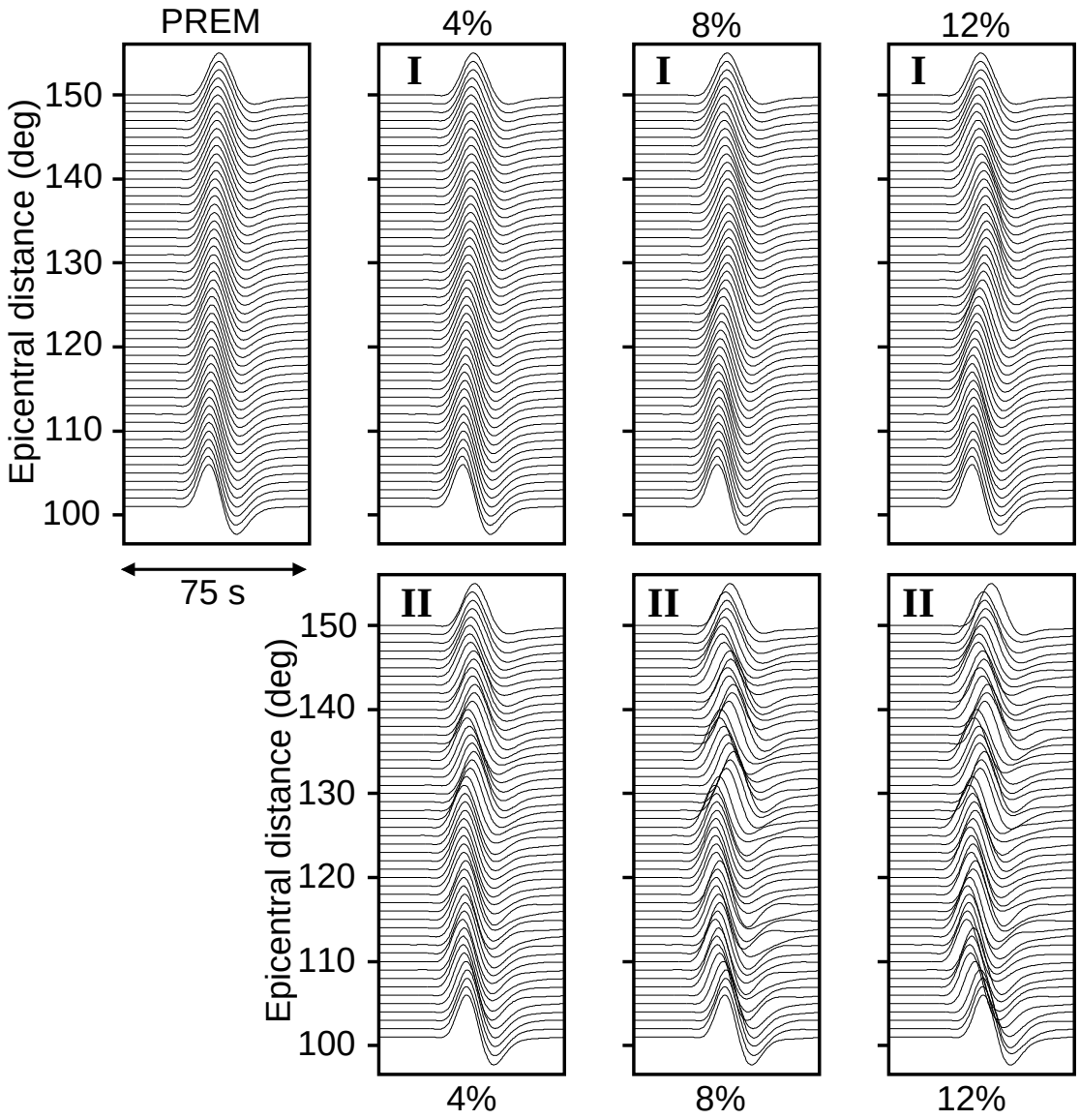

Figure 10: FD seismograms for the S_{diff} phase (dominant period 25 seconds) and the PREM model (top left), with heterogeneity according to spectral types I and II superimposed (right). The maximum perturbation is 0% (PREM), 4%, 8%, and 12%. Part of the 2-D models are shown in Figure 9.

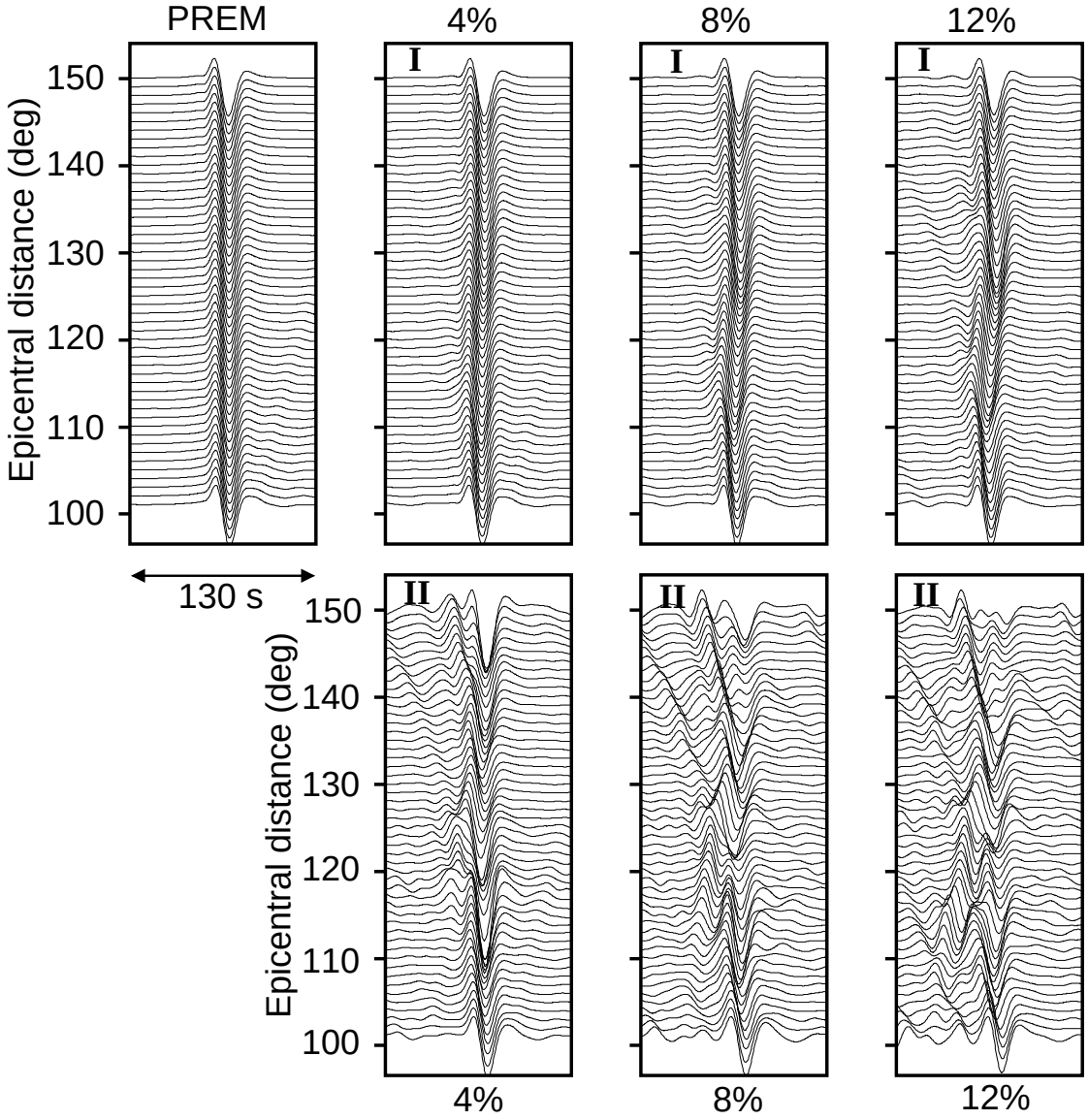

Figure 11: FD seismograms for the SS phase (dominant period 25 seconds) and the PREM model (top left), with heterogeneity according to spectral types I and II. superimposed (right). Same models as in Figure 10.

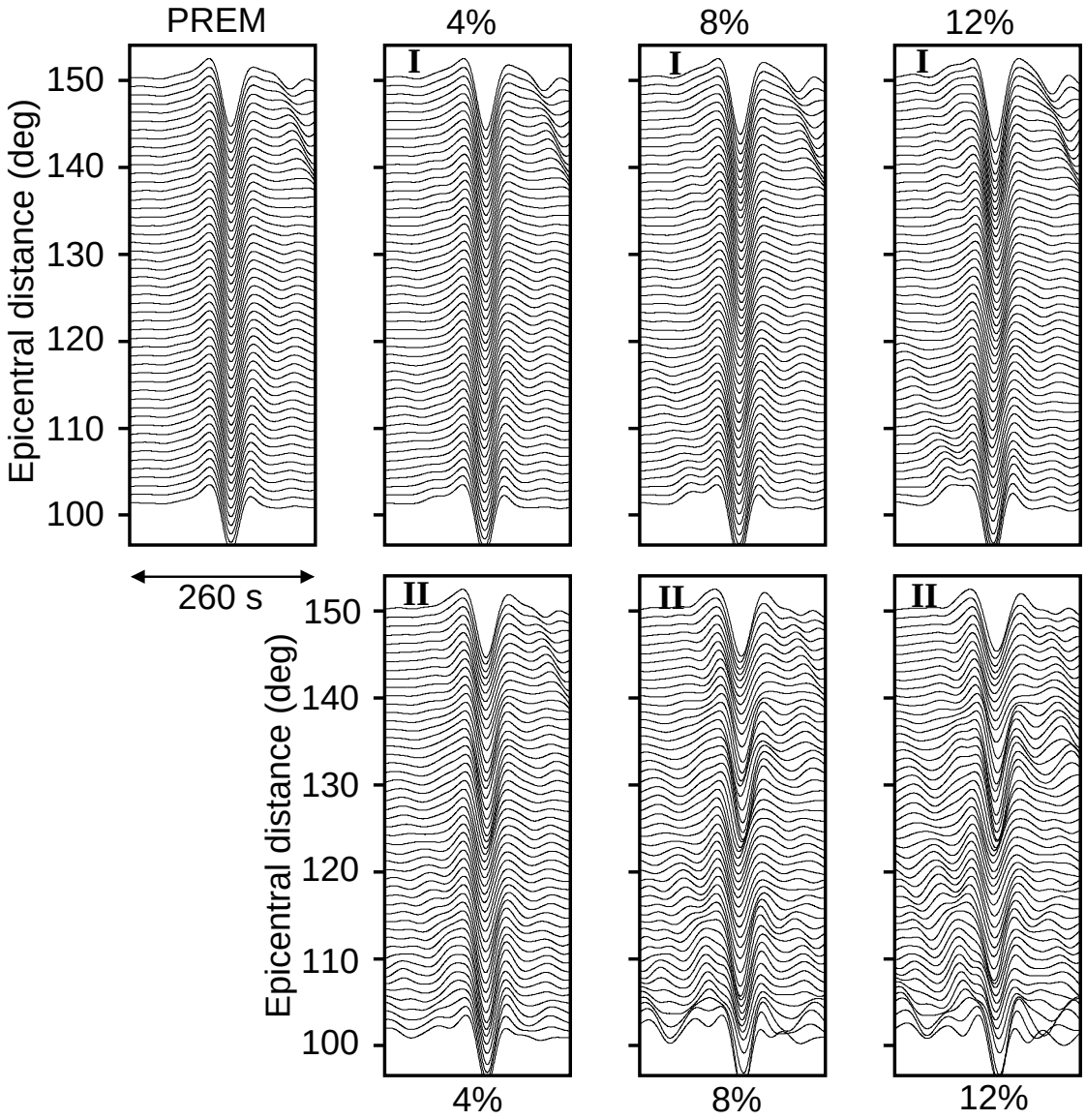

Figure 12: FD seismograms for the SS phase (dominant period 75 seconds) and the PREM model (top left), with heterogeneity according to spectral types I and II. superimposed (right). Same models as in previous Figure.

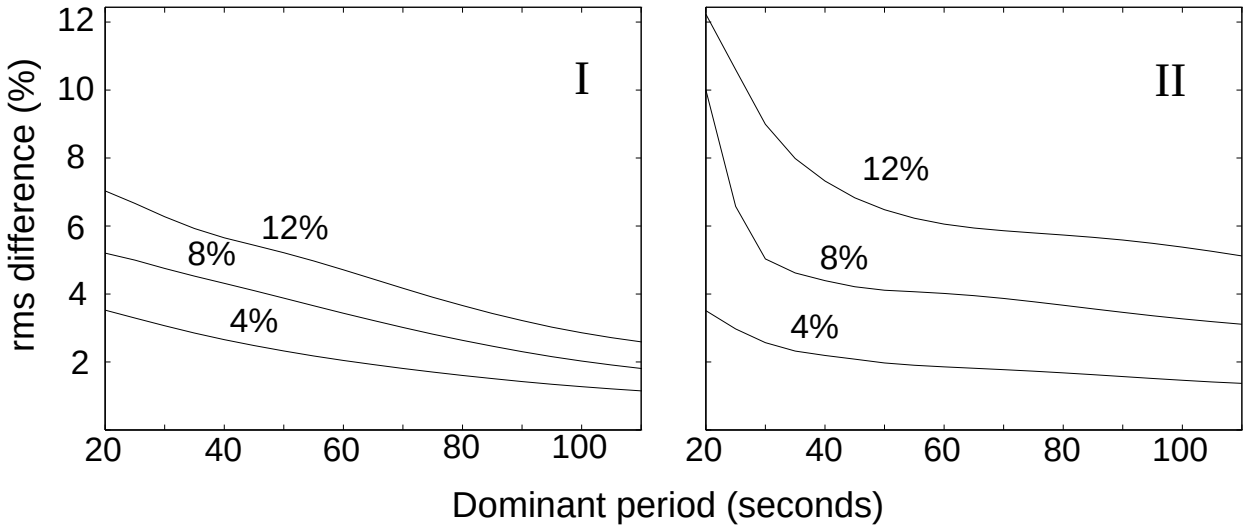

Figure 13: The mean scattering index $s(T)$ (defined in the text) as a function of dominant period for 5 simulations of each model type. Results are shown for the two types (I and II) of spectra and different maximum perturbation amplitude (4, 8, and 12%). Spectral type II is characterized by a rapid increase of waveform distortion at dominant periods $\leq$30 seconds.

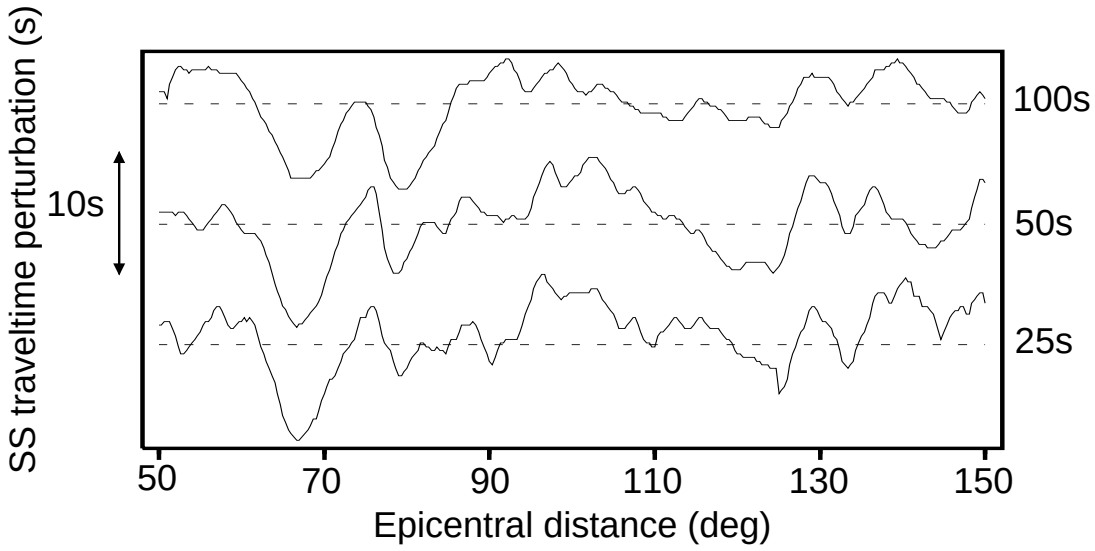

Figure 14: SS travel-time perturbations determined from seismograms of varied dominant period (25, 50, and 100 seconds) between 50 and 150 degrees epicentral distance. The receiver spacing is 1/3 degrees.

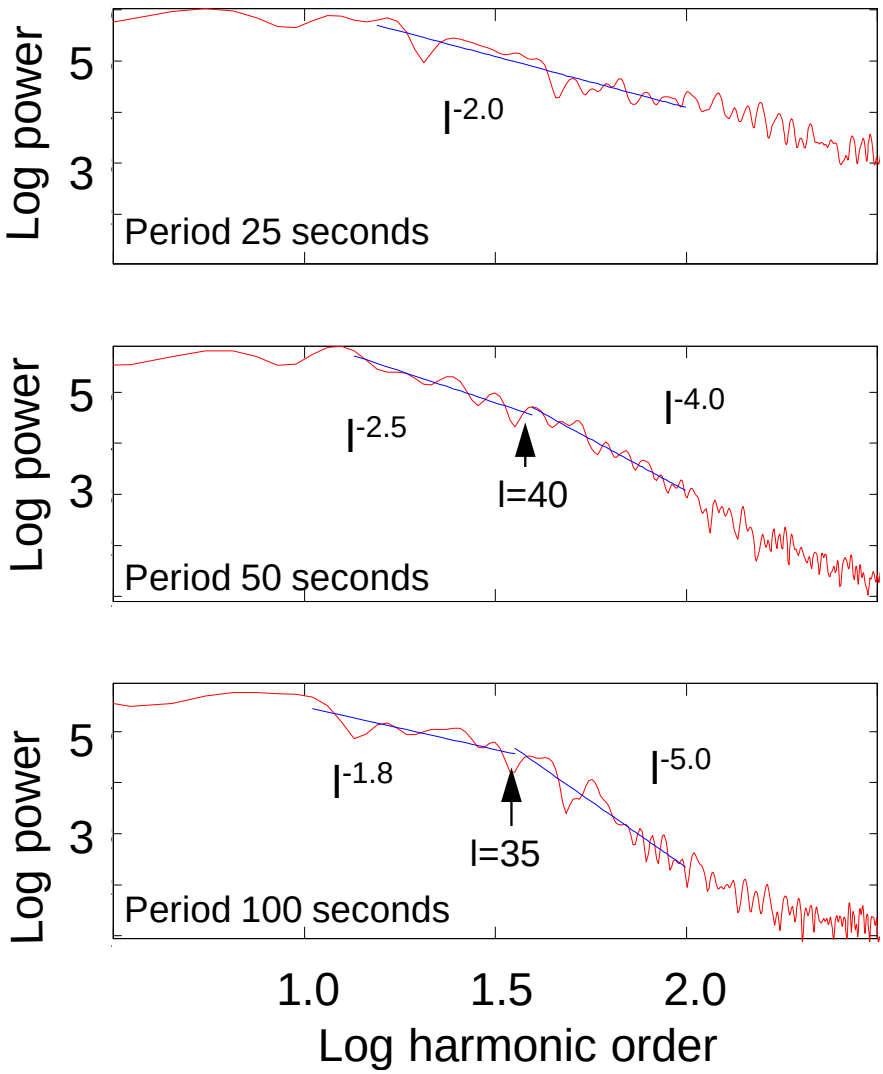

Figure 15: Power spectra of SS travel-time fluctuations determined in different frequency bands. In each case spectra for 5 random realizations using Earth models with identical characteristics are stacked. The model spectra are as in Figure 8 (lower). The underlying model perturbations have a corner at $l = 20$ and a slope of l^{-2}. The maximum model perturbation is 6%. Lines are fitted in various intervals. With increasing period the corner shifts towards lower orders and the decay rate in particular for order $l \geq 40$ increases.

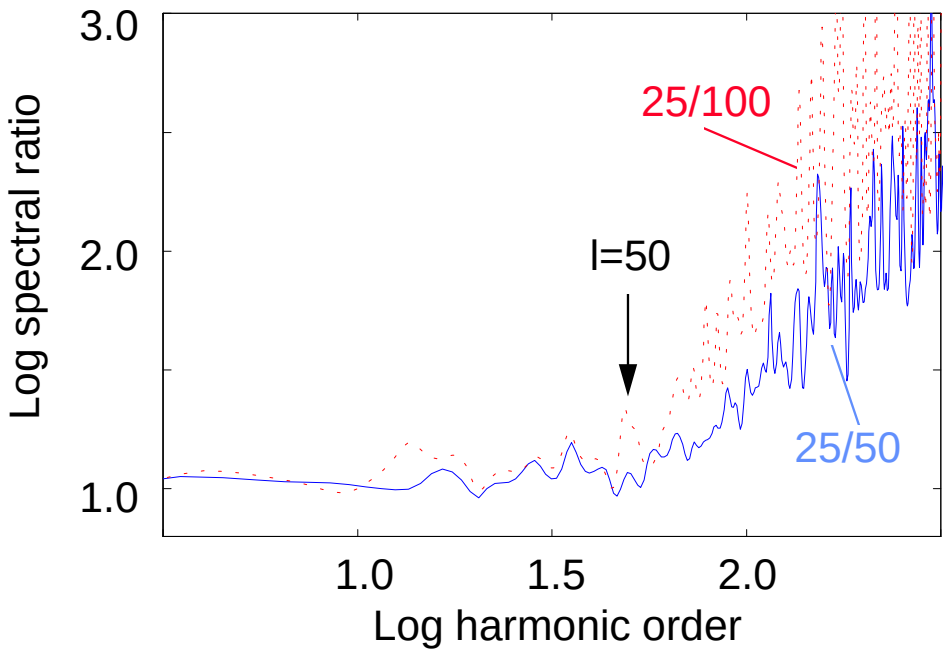

Figure 16: Spectral power ratio of the results shown in Figure 15. Solid line: ratio of power spectrum for dominant period of 25 seconds divided by power spectrum for dominant period of 50 seconds. Dashed line: Spectrum for 25 seconds divided by spectrum for 100 seconds period.

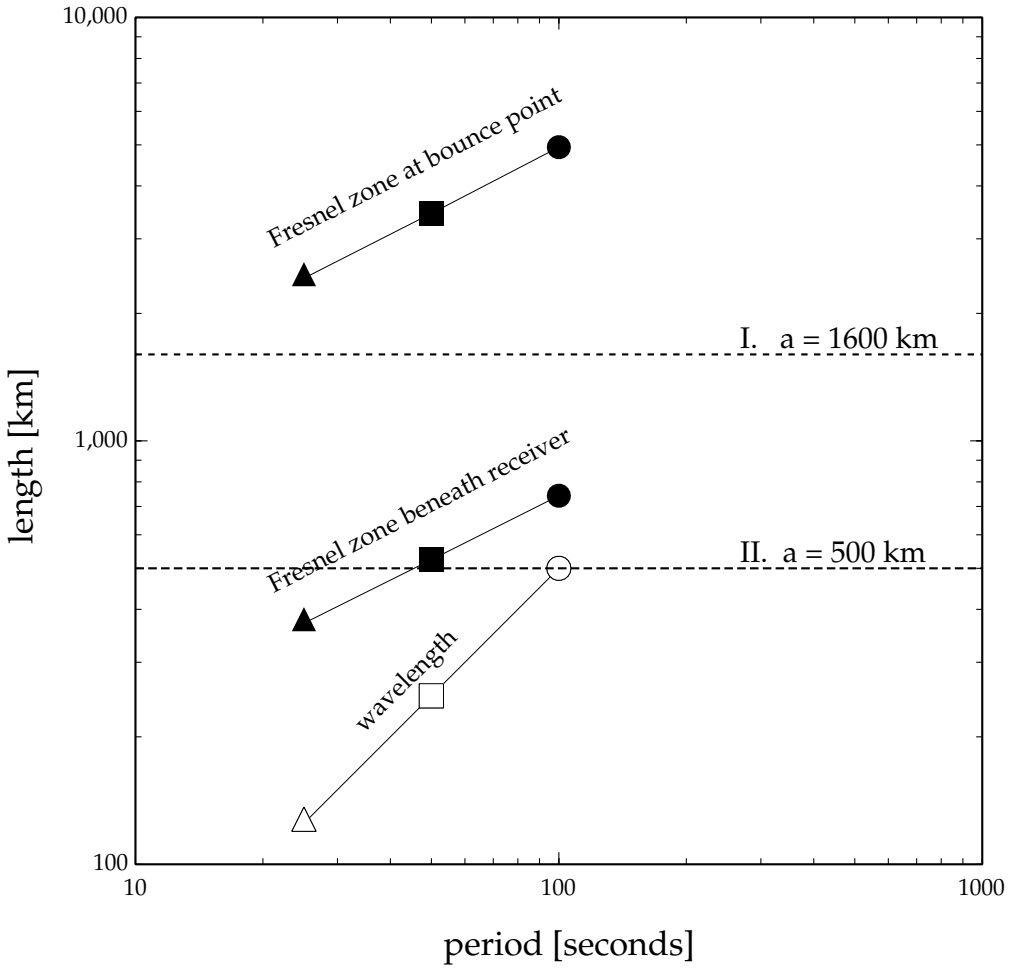

Figure 17: Classification of our SS-wave simulations in terms of period and the lengths scales which control scattering phenomena: the scale length of heterogeneity and the widths of the relevant Fresnel zone. The dashed horizontal lines are the correlation lengths for model types I and II. The solid symbols represent the widths of the first Fresnel zone for the three dominant periods we examined immediately beneath the receiver and around the surface bounce points.